

Beyond-Hubbard pairing in a cuprate ladder

Hari Padma¹, Jinu Thomas^{2,3}, Sophia TenHuisen¹, Wei He⁴, Ziqiang Guan¹, Jiemin Li⁵,
Byungjune Lee^{6,7}, Yu Wang⁸, Seng Huat Lee⁸, Zhiqiang Mao⁸, Hoyoung Jang⁹,
Valentina Bisogni⁵, Jonathan Pellicciari⁵, Mark P. M. Dean⁴, Steven Johnston^{2,3},
Matteo Mitrano¹

¹Department of Physics, Harvard University, Cambridge, MA, USA.

²Department of Physics & Astronomy, University of Tennessee, Knoxville, TN, USA.

³Institute of Advanced Materials and Manufacturing, University of Tennessee, Knoxville, TN, USA.

⁴Condensed Matter Physics and Materials Science Department, Brookhaven National Laboratory,
Upton, NY, USA.

⁵National Synchrotron Light Source II, Brookhaven National Laboratory, Upton, NY, USA.

⁶Department of Physics, Pohang University of Science and Technology, Pohang, Korea.

⁷Max Planck POSTECH/Korea Research Initiative, Center for Complex Phase Materials, Pohang,
Korea.

⁸2D Crystal Consortium, Pennsylvania State University, University Park, PA, USA.

⁹PAL-XFEL, Pohang Accelerator Laboratory, POSTECH, Pohang, Korea.

Supplemental Material

1. **Hole doping and charge order**
2. **Analysis of RIXS spectra**
3. **DMRG calculations**

1. Hole doping and charge order

The total fluorescence yield x-ray absorption spectroscopy and resonant soft x-ray scattering measurements were conducted at the RSXS endstation at the PAL-XFEL [1]. Samples were polished and mounted on a 6-axis in-vacuum manipulator. The incident x-rays were π -polarized and fluorescence and scattering signals were detected using avalanche photodiode point detectors. We corrected the x-ray absorption spectra for self-absorption effects using the package *Larch* [2]. The algorithm employs a method developed by D. Haskell [3], which applies an analytical correction based on the stoichiometry of the material and the incoming and outgoing x-ray angles. The magnitude of the effects was found to be of order 2%.

$\text{Sr}_{14}\text{Cu}_{24}\text{O}_{41}$ is composed of Cu_2O_3 two-legged ladder and CuO_2 chain structural subunits separated by Sr layers. The ladders and chains have identical lattice parameters along the a and b direction, but are incommensurate along the c axis ($c_L = 3.92 \text{ \AA}$, $c_C = 2.73 \text{ \AA}$). Assuming formal charges of Sr^{2+} and O^{2-} , $\text{Sr}_{14}\text{Cu}_{24}\text{O}_{41}$ has a nominal average Cu valence of +2.25, with the excess holes shared between Cu atoms in the ladder and chain subunits[4]. The hole density on the ladder is reported to be 0.06 holes/Cu, as quantified via O K -edge x-ray absorption spectra in previous studies [5]. In Fig. S1, we plot the normalized x-ray absorption spectra measured on our samples, together with previous measurements by Nucker, *et al.* [5]. The datasets are in excellent agreement, particularly at the chain and ladder mobile carrier pre-peaks which encode information about the hole distribution. This confirms that the hole density of the ladder sublattice in our samples is 0.06 holes/Cu.

Our resonant soft x-ray scattering measurements show a sharp charge order peak resonant with the ladder mobile carrier pre-peak at 528.6 eV, at a momentum transfer $(0, 0, 0.2 \pm 0.014)$ r. l. u. (see Fig. S2). We note that this momentum transfer is accessed using a different geometry than that used for the RIXS measurements. The charge order intensity decreases with increasing temperature, and vanishes at $T_{\text{CO}} = 255 \text{ K}$. The peak position and FWHM are independent of temperature. Our results are consistent with previous measurements [6], further confirming ladder hole density and the high quality of our single crystals.

2. Analysis of RIXS spectra

RIXS intensity map

Cu ions in $\text{Sr}_{14}\text{Cu}_{24}\text{O}_{41}$ experience two different bonding environments, namely corner-sharing CuO_4 plaquettes in the ladders and edge-sharing plaquettes in the chains. As a consequence of this inequivalence of the Cu sites, the ladders and chains resonate at different energies in the Cu L -edge x-ray absorption spectra [7] (see Fig. S3a). The corner-sharing ladders resonate at 932.5 eV, and the doped holes in the edge-sharing chain resonate at 934.4 eV. The resonance of the undoped sites in the chain likely overlaps with the ladder resonance at 932.5 eV. However, the chain contribution here is much smaller than that of the ladders [7, 8]. Hence, while we cannot exclude a small contribution from the chains, we may reasonably assume that the RIXS spectra resonant at 932.5 eV are dominated by ladder excitations.

We measure RIXS spectra as a function of the incident x-ray energy, shown in Fig. S3b. We find that the two-triplon and dd excitations resonate only at the incident energy corresponding to the XAS peak at 932.5 eV, with negligible intensity at the incident energy corresponding to that of the doped holes on the chain at 934.4 eV.

RIXS intensity due to quasiparticle spin flips

In Fig. 2b of the main text, we highlight the contribution of quasiparticle (QP) spin flips to the RIXS intensity at 260 K, and at one representative momentum. Here, we describe the fitting procedure and show fits to spectra at additional representative momenta, measured at both 40 K and 260 K. The RIXS spectra below 0.7 eV exhibit several spectral features, including an elastic line, a phonon, its second harmonic, and a broad two-triplon continuum. At 260 K, an additional spectral feature, originating from QP spin flips, is evident at the low energy shoulder of the two-triplon continuum, particularly near the zone boundary. This feature closely follows the downward dispersion of the two-triplon continuum, and is only present above T_{CO} , thus ruling out its assignment as a higher harmonic of the phonon. We fit the elastic, phonon, and QP spin flip features to Gaussian lineshapes. The two-triplon continuum is not a single mode, but its shape can be reproduced phenomenologically by the sum of an asymmetric Lorentzian and a Gaussian. We show the fit results at four representative momenta, measured at 40 K and 260 K, in Fig. S6. The QP spin flip

feature, highlighted in dark grey, is small or absent in the 40 K spectra (Fig. S6(a-d)). In contrast, the QP spin flip peak is prominent in the 260 K spectra (Fig. S6(e-h)), and disperses together with the low energy shoulder of the two-triplon continuum, consistent with theoretical predictions [9, 10].

Finally, we confirm that the QP excitation is indeed a spin-flip excitation. We first obtained the amplitude of the QP feature at 260 K for $|L| = 0.35$ to 0.50, where it is clearly discernible, by fitting the spectra (see Fig. S6(e-h) for representative fits). We then computed the spin-flip and non-spin-flip cross section using the EDRIXS package [11] (see Fig. S8(d)). Normalizing the amplitude assuming the QP feature is from a spin-flip process yields similar intensity at $\pm L$, consistent with this feature coming from the dynamical spin structure factor $S(q, \omega)$, as shown in Fig. S9. If we instead assume that the QP feature is from a non-spin flip process, we obtain the unphysical result of $N(q, \omega)$ (or $S_{\text{exch}}(q, \omega)$ [10]) being significantly different at symmetric $\pm L$ values.

Extracting $S(q, \omega)$ from the RIXS intensity

The first step to convert the raw resonant inelastic x-ray scattering (RIXS) spectra (see Figs. S4 and S5) into dynamical spin structure factors is to subtract the non-magnetic components of the scattered signal. As shown in Fig. 2(b) of the main text, we fit to Gaussian lineshapes and subtract the elastic line, the 60-meV phonon, and its second harmonic at 120 meV.

Next, we normalize the subtracted RIXS spectra by scaling them by a geometry-dependent factor to ensure that the integrated intensity of the orbital excitations matches the theoretical single-ion scattering cross-section calculated using exact diagonalization (ED) [11]. For this, we consider pure orbital excitations of a Cu^{2+} ion in a square-planar crystal field, neglecting spin-flip and phonon contributions. In these calculations, x , y , and z are parallel to the crystallographic a , c , and b directions, respectively. We fix the theoretical crystal field parameters to match the experimental orbital excitation energies (neglecting the small dispersion of the $d_{xz/yz}$ orbital, see Fig. 4), and obtain $D_q = 0.164$ eV, $D_s = 0.42$ eV, and $D_t = 0.19$ eV, consistent with the crystal field parameters of corner-sharing plaquettes without apical oxygens [12]. The experimental and calculated RIXS spectra as a function of incident angle θ are shown in Fig. S8(a) and S8(b). We multiply the experimental spectra in Fig. S8(a) by a θ -dependent scaling

factor to match the integrated orbital intensity of the calculated spectra, plotted as a function of θ in Fig. S8(c). We refer to these as ‘normalized RIXS spectra’.

Finally, we extract the dynamical spin structure factor $S(\mathbf{q}, \omega)$. The intensity of RIXS magnetic excitations is proportional to $S(\mathbf{q}, \omega)$ multiplied by the atomic form factor of the single-ion spin-flip amplitude $R_{\text{spin}}(\epsilon, \epsilon', \Omega_i)$, where ϵ and ϵ' are the polarization of the initial and final photons, and the Ω_i is the excitation energy [13, 14]:

$$I_{\text{spin}} \propto R_{\text{spin}}(\epsilon, \epsilon', \Omega_i) \times S(\mathbf{q}, \omega).$$

While this formalism does not account for doping, it has been shown that this correspondence is also applicable for doped systems within the energy range of magnetic excitations [15]. We calculate $R_{\text{spin}}(\epsilon, \epsilon', \Omega_i)$ for a single hole in a $d_{x^2-y^2}$ orbital with its spin oriented along the in-plane diagonal direction $[1, 0, 1]$ and π polarized incident x-rays, following the approach outlined in previous work [13, 16]. The calculated spin-flip scattering cross-section as a function of θ is shown in Fig. S8(d). We obtain $S(\mathbf{q}, \omega)$ (up to an overall scaling factor) by dividing the normalized RIXS spectra by R_{spin} .

Orbital dispersion and Kugel-Khomskii model

We assign the RIXS orbital excitation peaks (see representative example in Fig. 4(a)) by using our single-site ED calculations outlined in the previous section. To visualize the dispersion of these excitations, we normalize the spectra to the integrated intensity between 1.4 eV and 3 eV and plot the data as a momentum-energy map in Fig. 4(b). We observe a clear dispersion in the lower branch of the $d_{xz/yz}$ excitation. The d_{xy} and $d_{3z^2-r^2}$ branches are dispersionless. We additionally note a weak, dispersing shoulder at an energy loss of around 2.3 eV that is apparent only near the zone boundary.

We focus on the lower branch of the $d_{xz/yz}$ excitation, which is intense, well separated from other peaks, and shows a clear dispersion. The momentum-dependent orbital excitation spectra are fit to three peaks, neglecting the weak shoulder at 2.3 eV: a skewed Gaussian lineshape for the d_{xy} branch, and Gaussian lineshapes for the $d_{xz/yz}$ and $d_{3z^2-r^2}$ branches.

The center of the $d_{xz/yz}$ peak extracted from the fits is plotted as a function of momentum in Fig. 4(c), showing a dispersion of around 80 meV. The particular shape of the dispersion, with a maximum at the zone center and minima at approximately $\pm\pi/2$ is consistent with spin-orbital separation [17–19]. Spin-orbital separation can be theoretically described using the Kugel-Khomskii model [20]. In this model, the lower branch of a propagating orbitalon has a characteristic dispersion of the form $E(q) = E_0 - 2J_o \sin(q)$, where E_0 is the on-site energy of the $d_{xz/yz}$ orbital, J_o is the orbital exchange constant, and q is the momentum transfer along the L direction. Fitting the dispersion of the $d_{xz/yz}$ excitation to this model, we obtain $E_0 = 2.013 \pm 0.007$ eV and $J_o = 22.5 \pm 5.4$ meV (see Fig. 4(b)).

Finally, we note that the large orbital dispersion of 80 meV rules out their origin being in the chains. This is because the inter-plaquette hopping t in edge-sharing chains (Cu-O-Cu bond angle of 90°) is much smaller than that in corner-sharing networks (Cu-O-Cu bond angle of 180°). As a consequence, the dispersion of orbital excitations, determined by the orbital superexchange $J_o \propto t^2$, will be an order of magnitude smaller in edge-sharing chains. The value $J_o = 22$ meV extracted from our results is of the same order of magnitude as in other corner-sharing systems (e. g. Sr_2CuO_3 chains: 75 meV [17], CaCuO_2 planes: 15 meV [21]). These observations, together with the fact that the orbital dispersion periodicity matches the ladder Brillouin zone, strongly suggest that the orbital dispersion originates in the corner-sharing ladders.

3. DMRG calculations

Dynamical spin structure factors with V

Fig. S10 shows the $S(\mathbf{q}, \omega)$ for various values of V computed in a 64×2 cluster. The model parameters are the same as above, with the modification that U and V are simultaneously changed to ensure $U - V = 8t$. We find that positive (repulsive) V and small values of negative (attractive) V leave the spectra unchanged, with two-triplon excitations and an intense low-energy branch corresponding to the quasiparticle spin-flip excitations. However, further increasing the value of negative V monotonically depletes the quasi-particle spin-flip scattering intensity. Larger negative values of V also increase the paired holes tendency to collect near the boundaries of the cluster, consistent with previous results [22]. This behavior can be linked to their increased effective mass, which makes them more prone to localization. In this case, the boundary of the cluster creates a weak pinning potential, akin to an impurity. We have verified that any weak pinning potential in the cluster is sufficient to achieve this effect [23], including any incommensuration generated by the chains in $\text{Sr}_{14}\text{Cu}_{24}\text{O}_{41}$.

Pair Correlations

We examine the effect of V on the superconducting correlations by calculating the rung-rung singlet pair correlation function

$$P_{r,r}(d) = \langle \Delta_r^\dagger(c) \Delta_r(c+d) \rangle, \quad (1)$$

where the rung-singlet pair operator $\Delta_r(i) = \frac{1}{\sqrt{2}}(c_{i,1,\uparrow}c_{i,2,\downarrow} - c_{i,1,\downarrow}c_{i,2,\uparrow})$, as a function of distance from the center site c of the cluster. Fig. S11(a) plots the pair correlations at longer distances for representative values of $-|V|$. We find that $P_{r,r}(d)$ increases and begins to saturate at large distances as the attractive interaction is made stronger, consistent with the findings of reference [22]. These results indicate that the attractive next-nearest-neighbor interaction enhances the long-range superconducting correlations in the system.

We also investigate the pairing symmetry of the ladder with $|V| \neq 0$ by comparing the rung-rung to the rung-leg pair correlations

$$P_{r,l}(d) = \langle \Delta_r^\dagger(c) \Delta_l(c+d) \rangle, \quad (2)$$

where $\Delta_l(i) = \frac{1}{\sqrt{2}}(c_{i,1,\uparrow}c_{i+1,1,\downarrow} - c_{i,1,\downarrow}c_{i+1,1,\uparrow})$ destroys the singlet pair along the leg of the ladder. When $|V| = 0$, $P_{r,r}$ and $P_{r,l}$ have the opposite sign, consistent with a d -wave-like pairing symmetry [24]. Our results show that this symmetry persists once $|V| \neq 0$, as shown in Fig. S11(b).

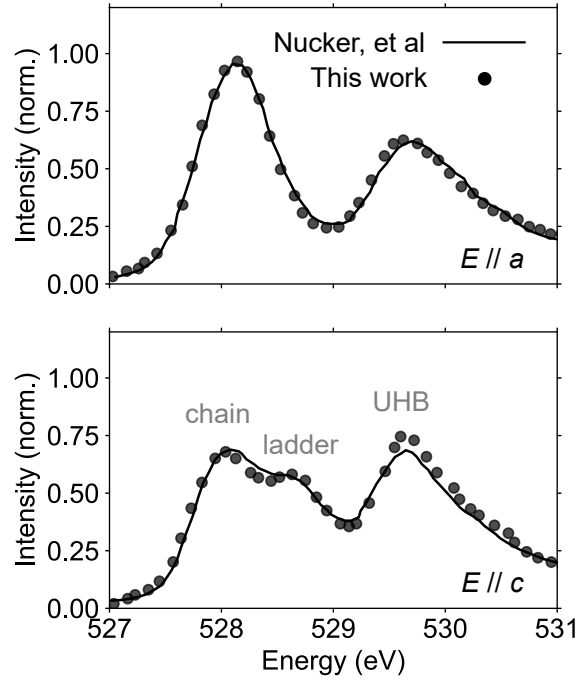


FIG. S1. O K -edge x-ray absorption spectra. Total fluorescence yield O K -edge x-ray absorption spectra measured on our samples and corrected for over-absorption (circles), overlaid on data measured by Nucker, et al [5] (solid lines), for incident x-ray polarization along the a (top) and c (bottom) directions. The chain and ladder mobile carrier prepeaks and the upper Hubbard band (UHB) peak are labeled. The spectra are in excellent agreement with each other, confirming the hole density of 0.06 holes/Cu in our samples.

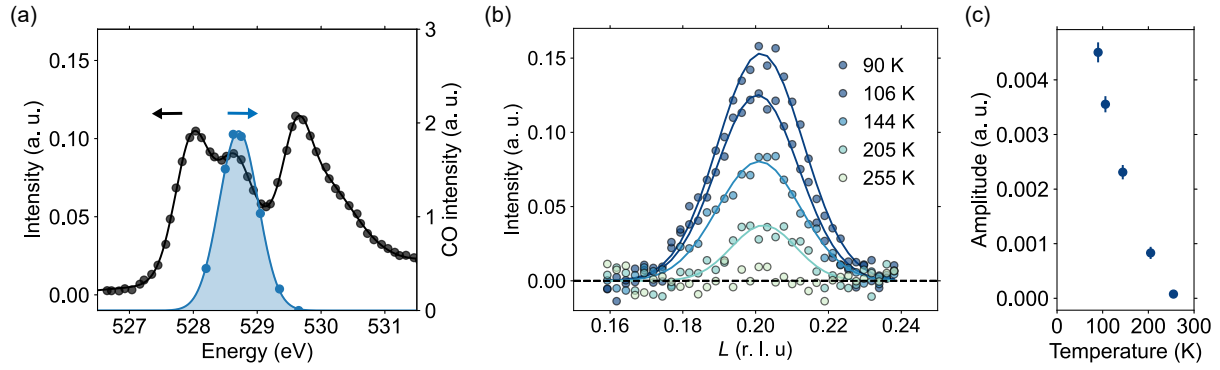


FIG. S2. Charge order resonant with ladder holes. (a) Charge order (CO) intensity as a function of incident x-ray photon energy (blue circles), overlaid on the O K-edge x-ray absorption spectrum with polarization along the c direction (black circles). The CO peak is resonant with the ladder mobile carrier prepeak. (b) The CO diffraction peak at $(0, 0, 0.20)$ r. l. u. at various temperatures. (c) The integrated intensity of the CO peak plotted as a function of temperature. The intensity vanishes at 255 K. The solid lines are fits to Gaussian lineshapes. r. l. u.: reciprocal lattice units

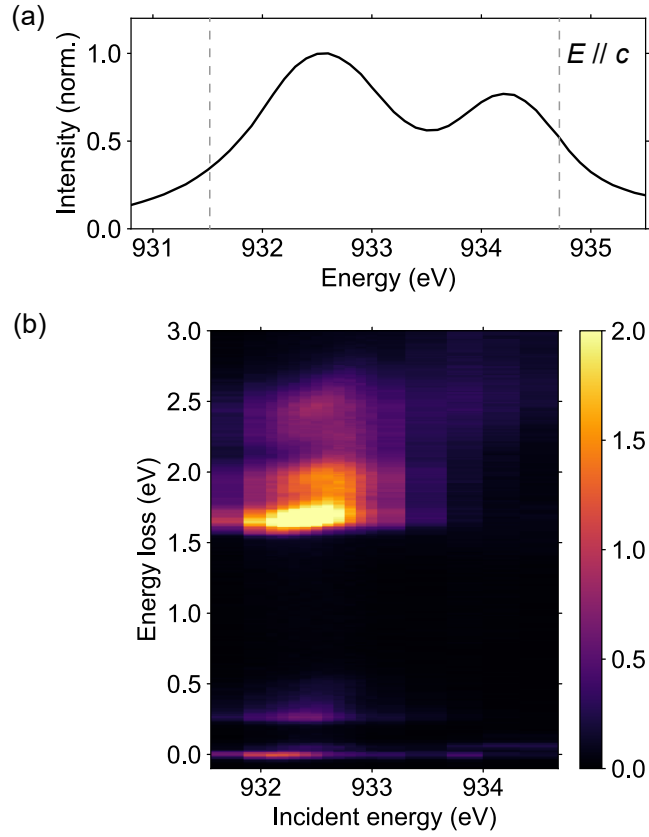


FIG. S3. RIXS intensity map. (a) X-ray absorption spectrum at the Cu L_3 -edge, with x-rays polarized parallel to c . The peaks centered at 932.5 eV and 934.4 eV correspond to contributions predominantly from the corner-sharing ladders and edge-sharing chains, respectively. Dashed grey lines denote the range over which the intensity map in panel (b) was measured. (b) RIXS signal as a function of the incident x-ray energy measured at $L = -0.35$ r. l. u. showing two-triplons (0.3 to 0.5 eV) and dd excitations (1.5 to 2.8 eV) resonating with the ladder peak. All data were collected at 40 K.

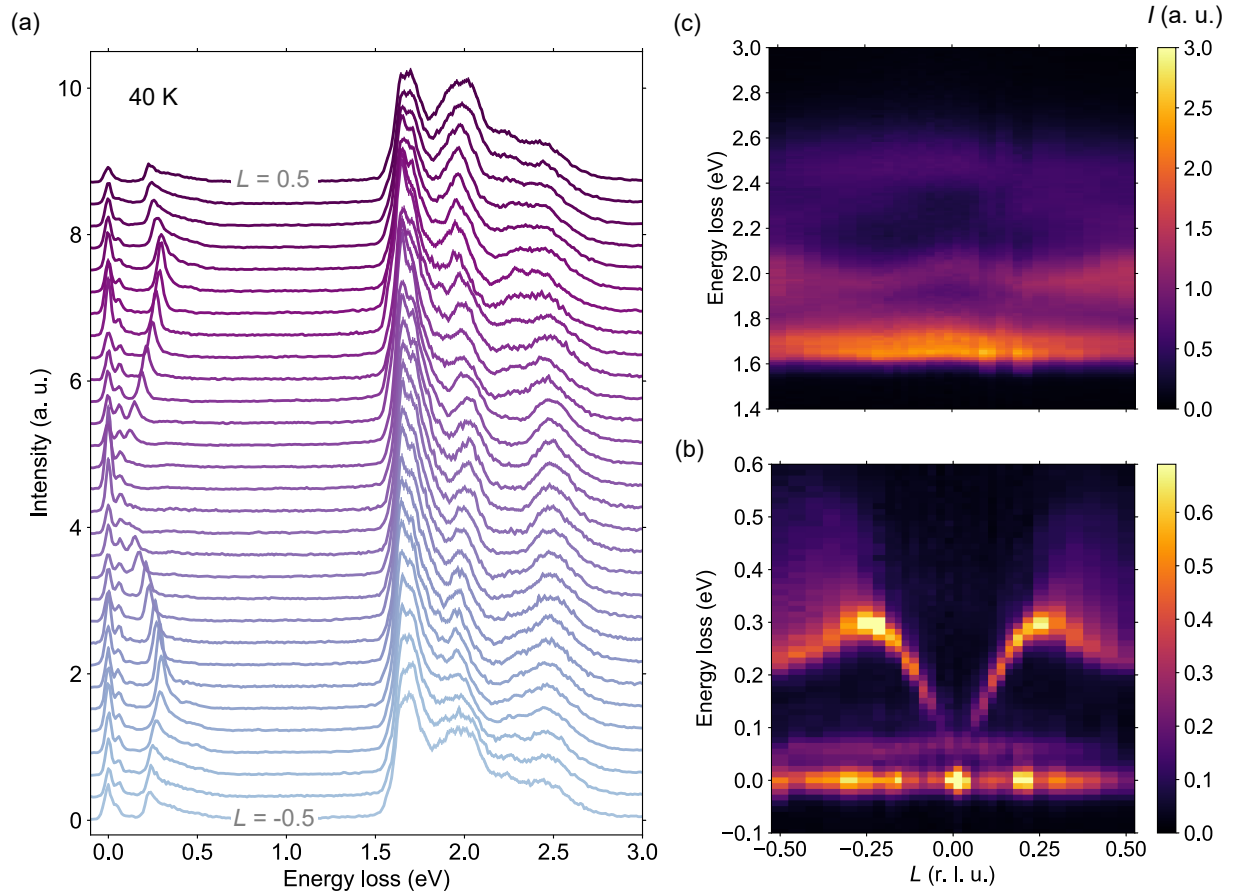


FIG. S4. Raw RIXS spectra at 40 K. (a) Raw RIXS spectra plotted as a function of momentum spanning $L = -0.5$ to 0.5 r. l. u. measured at 40 K. (b-c) Momentum-energy maps of RIXS spectra in the regions dominated by magnetic excitations (b) and orbital excitations (c).

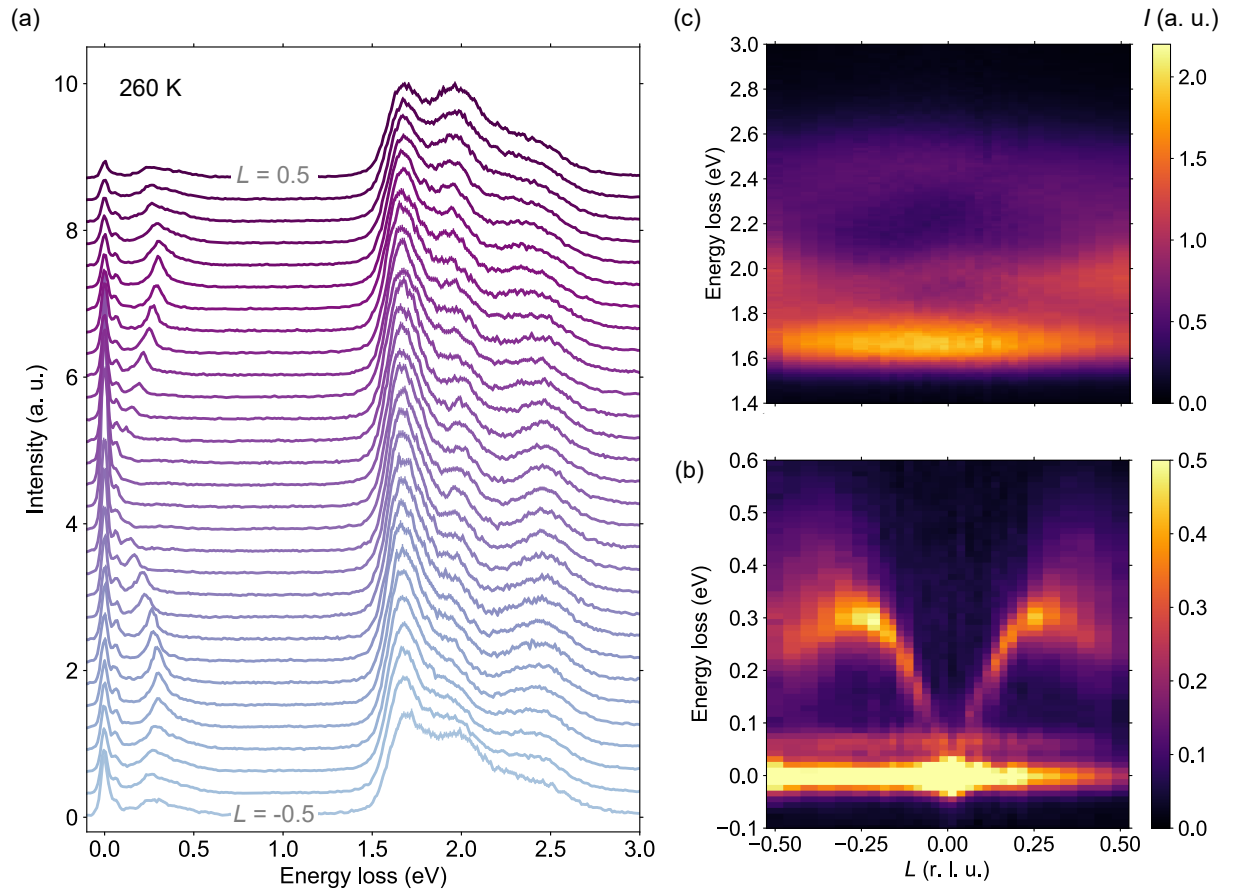


FIG. S5. Raw RIXS spectra at 260 K. (a) Raw RIXS spectra plotted as a function of momentum spanning $L = -0.5$ to 0.5 r. l. u. measured at 260 K. (b-c) Momentum-energy maps of RIXS spectra in the regions dominated by magnetic excitations (b) and orbital excitations (c).

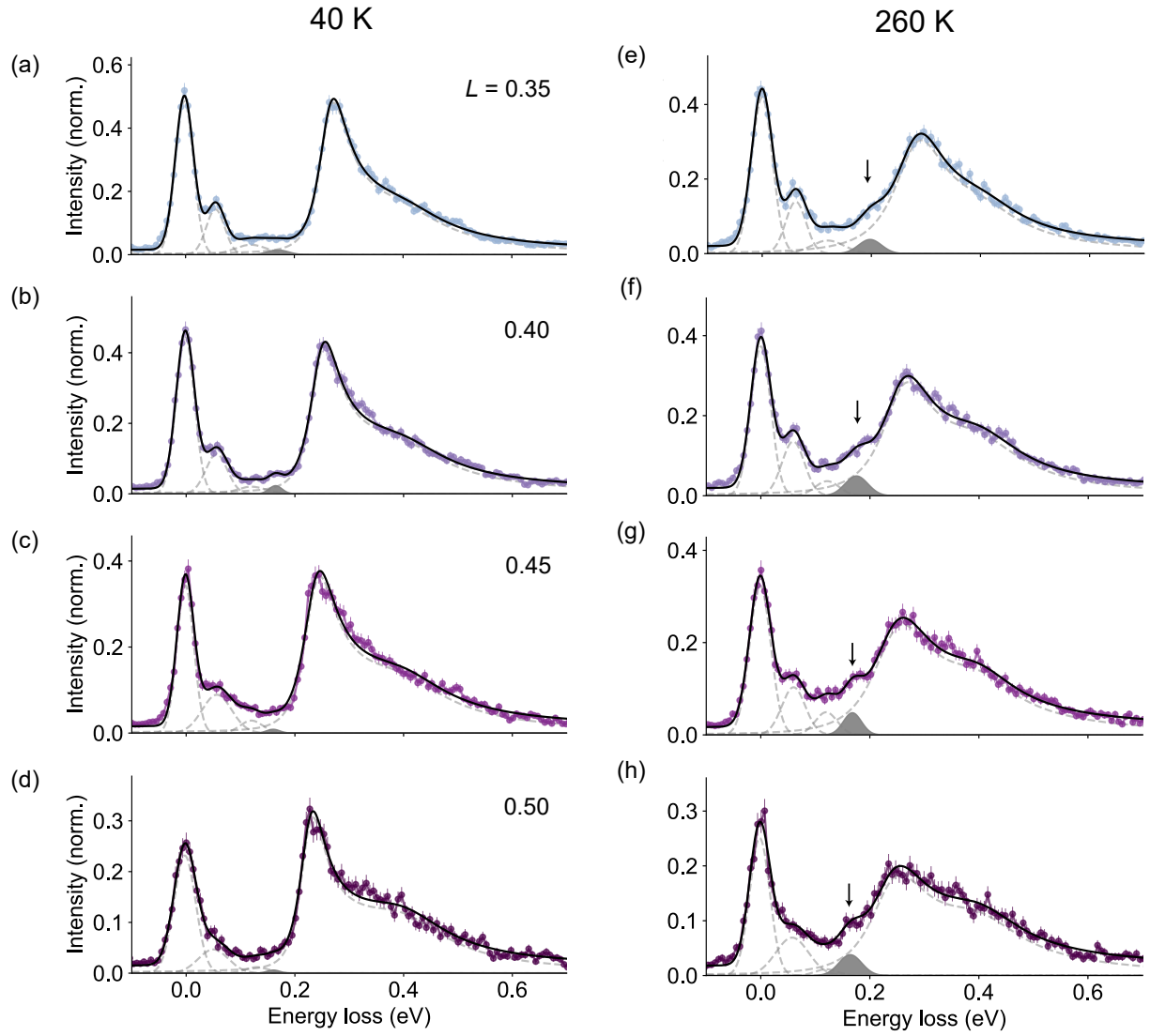


FIG. S6. Quasiparticle spin flip contribution to RIXS intensity. RIXS spectra measured at (a-d) 40 K and (e-h) 260 K, as a function of momentum $L = 0.35$ to 0.50 . The elastic, phonon, phonon harmonic, and quasiparticle spin flip features are fit to Gaussian lineshapes, and the two-triplon continuum is fit to the sum of an asymmetric Lorentzian and a Gaussian function. Black solid lines are the total fits, including a constant offset, grey dashed lines are individual contributions, and shaded dark grey regions are the quasiparticle spin flip contribution. The quasiparticle spin flip peaks are additionally indicated with arrows.

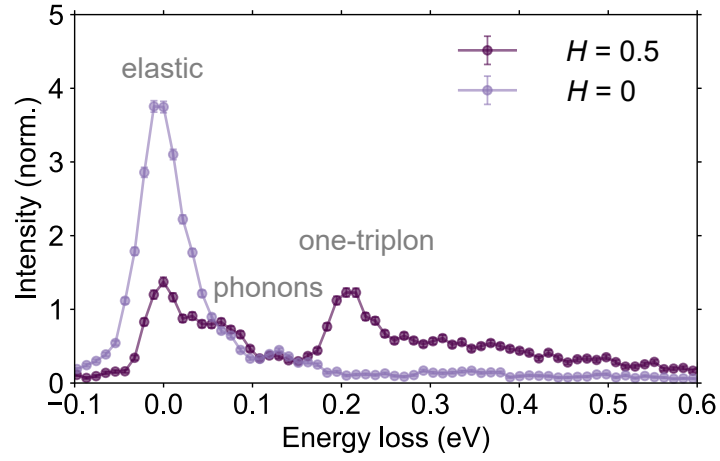


FIG. S7. One-triplon excitation. RIXS spectra measured at $H = 0.5$ and 0, with L fixed to 0. The elastic, phonon, and one-triplon peaks are labeled. The spectra are normalized to the phonon intensity for comparison. The one-triplon excitation is observed only at $H = 0.5$, as expected from symmetry considerations.

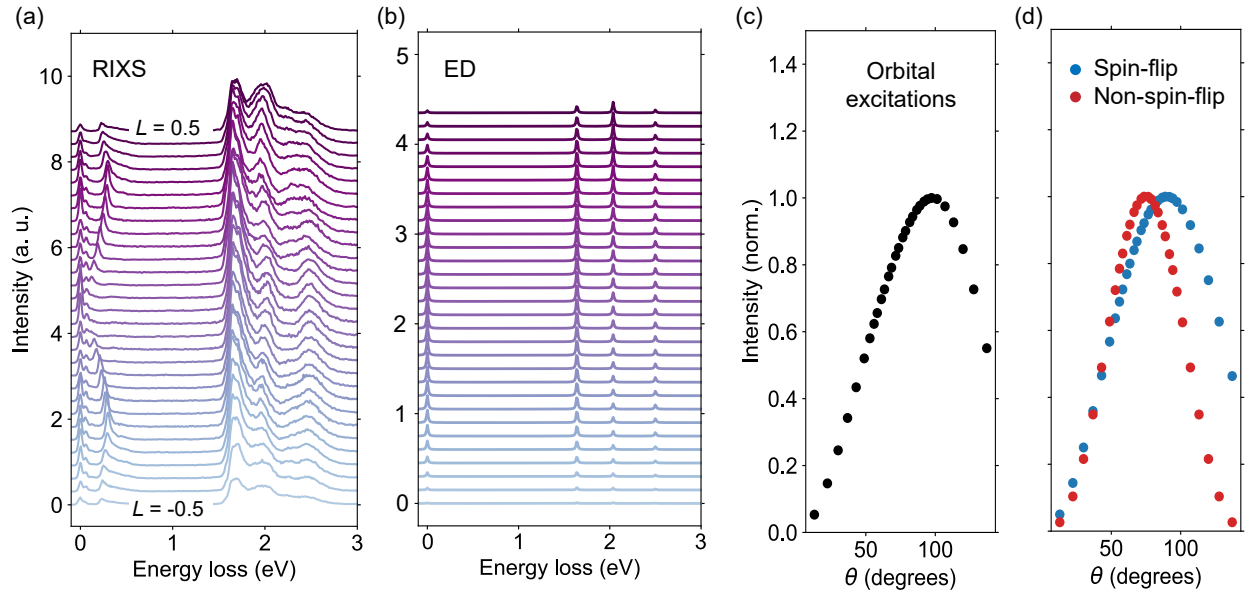


FIG. S8. Single-site calculations using ED. (a) The raw RIXS spectra measured as a function of momentum spanning $L = -0.5$ to 0.5 r. l. u. (b) Orbital excitation spectra calculated using ED for a single-site model. (c-d) RIXS scattering cross-sections calculated using ED. Integrated orbital excitation scattering cross-section (c), and spin-flip and non-spin-flip cross-sections (d) as a function of incident angle for π -polarized x-rays.

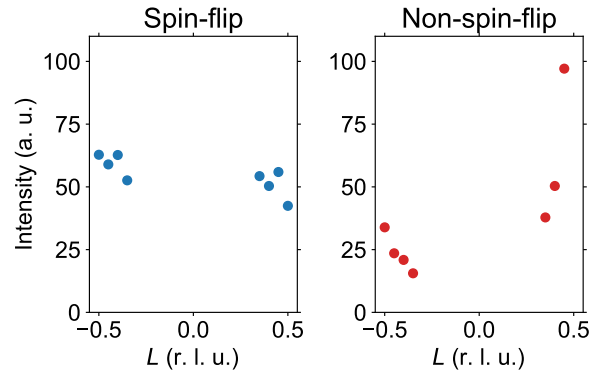


FIG. S9. Evidence for spin-flip nature of QP excitation. The $S(q, \omega)$ (left) and $N(q, \omega)$ (or $S_{\text{exch}}(q, \omega)$) (right) of the QP excitation amplitude extracted from the RIXS spectra, assuming it is a spin-flip and non-spin-flip process, respectively.

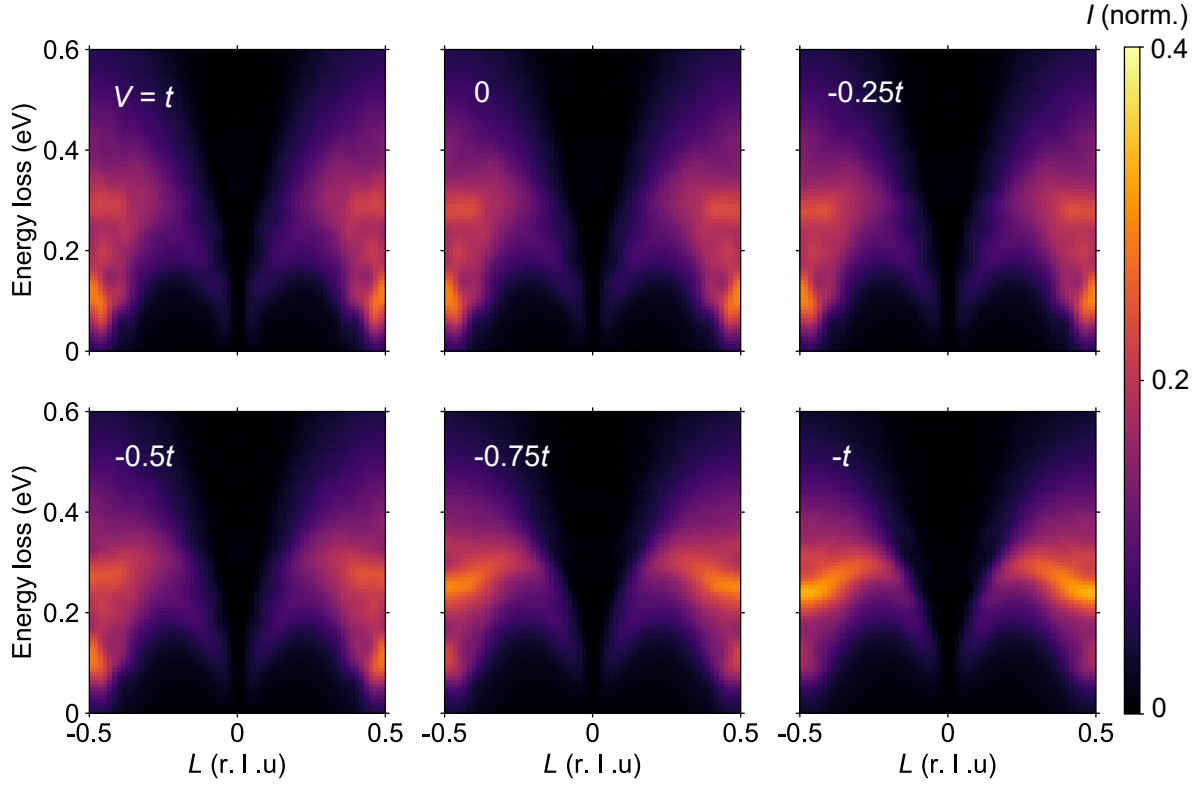


FIG. S10. Dynamical spin structure factors for varying V . Density matrix renormalization group (DMRG) calculations for the dynamical spin structure factor computed on a 64×2 cluster for the model parameters $t = 1$, $t_{\perp} = 0.84t$, $t' = 0.3t$, and $U - V = 8t$. V ranges from 1 to -1 and the broadening is set $\eta = 0.1t$.

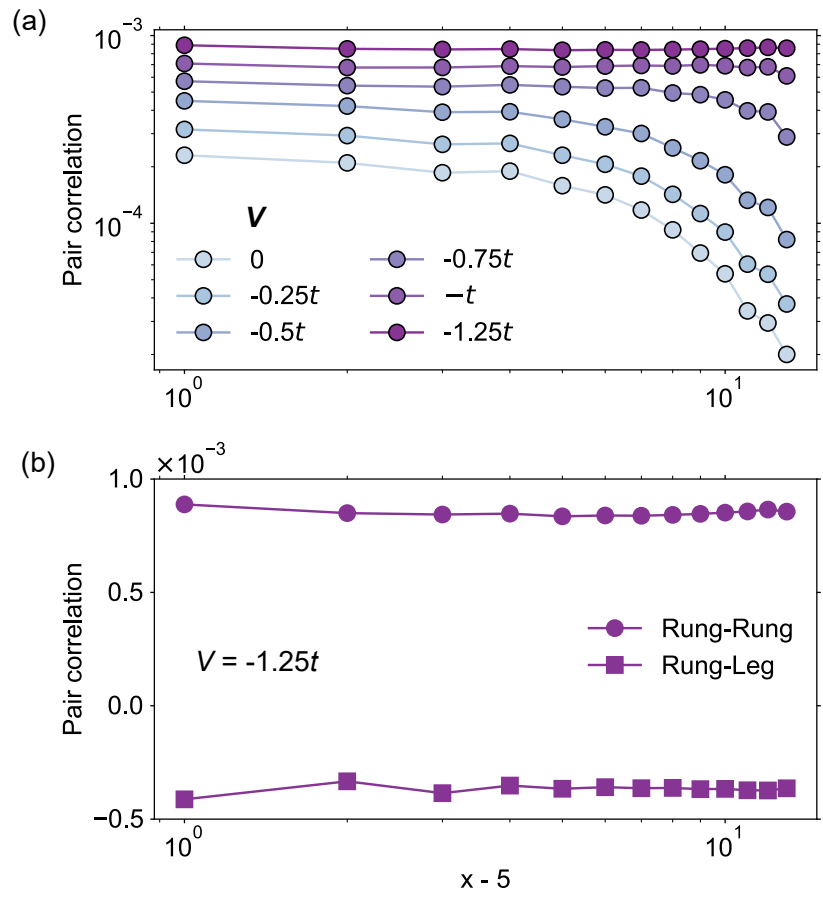


FIG. S11. Singlet pair correlations. (a) DMRG results for the rung-rung singlet pair correlations for various values of V . (b) Rung-rung and rung-leg singlet pair correlations for $V = -1.25t$. The sign change going from rung-rung to rung-leg directions indicates a d -wave-like character.

References

- [1] Jang, H. *et al.* Time-resolved resonant elastic soft x-ray scattering at Pohang Accelerator Laboratory X-ray Free Electron Laser. *Review of Scientific Instruments* **91**, 083904 (2020).
- [2] Newville, M. *Larch: an analysis package for xafs and related spectroscopies*, Vol. 430, 012007 (IOP Publishing, 2013).
- [3] Haskel, D. FLUO: Correcting XANES for self-absorption in fluorescence measurements (1999).
- [4] Osafune, T., Motoyama, N., Eisaki, H. & Uchida, S. Optical Study of the $\text{Sr}_{14-x}\text{Ca}_x\text{Cu}_{24}\text{O}_{41}$ System: Evidence for Hole-Doped Cu_2O_3 Ladders. *Physical Review Letters* **78**, 1980 (1997).
- [5] Nücker, N. *et al.* Hole distribution in $(\text{Sr}, \text{Ca}, \text{Y}, \text{La})_{14}\text{Cu}_{24}\text{O}_{41}$ ladder compounds studied by x-ray absorption spectroscopy. *Physical Review B* **62**, 14384 (2000).
- [6] Abbamonte, P. *et al.* Crystallization of charge holes in the spin ladder of $\text{Sr}_{14}\text{Cu}_{24}\text{O}_{41}$. *Nature* **431**, 1078–1081 (2004).
- [7] Huang, M.-J. *et al.* Determination of hole distribution in $\text{Sr}_{14-x}\text{Ca}_x\text{Cu}_{24}\text{O}_{41}$ using soft x-ray absorption spectroscopy at the Cu L_3 edge. *Physical Review B* **88**, 014520 (2013).
- [8] Hu, Z. *et al.* Doped holes in edge-shared CuO_2 chains and the dynamic spectral weight transfer in X-ray absorption spectroscopy. *Europhysics Letters* **59**, 135 (2002).
- [9] Troyer, M., Tsunetsugu, H. & Rice, T. Properties of lightly doped t - J two-leg ladders. *Physical Review B* **53**, 251 (1996).
- [10] Kumar, U., Nocera, A., Dagotto, E. & Johnston, S. Theoretical study of the spin and charge dynamics of two-leg ladders as probed by resonant inelastic x-ray scattering. *Physical Review B* **99**, 205130 (2019).
- [11] Wang, Y., Fabbris, G., Dean, M. P. M. & Kotliar, G. EDRIXS: An open source toolkit for simulating spectra of resonant inelastic x-ray scattering. *Computer Physics Communications* **243**, 151–165 (2019).
- [12] Sala, M. M. *et al.* Energy and symmetry of dd excitations in undoped layered cuprates measured by Cu L_3 resonant inelastic x-ray scattering. *New Journal of Physics* **13**, 043026 (2011).
- [13] Ament, L. J., Ghiringhelli, G., Sala, M. M., Braicovich, L. & van den Brink, J. Theoretical demonstration of how the dispersion of magnetic excitations in cuprate compounds can be determined using resonant inelastic X-ray scattering. *Physical Review Letters* **103**, 117003 (2009).
- [14] Roberts, H. C. *et al.* Dynamical spin susceptibility in La_2CuO_4 studied by resonant inelastic x-ray scattering. *Physical Review B* **103**, 224427 (2021).
- [15] Jia, C. *et al.* Persistent spin excitations in doped antiferromagnets revealed by resonant inelastic light scattering. *Nature Communications* **5**, 3314 (2014).
- [16] Shen, Y. *et al.* Role of oxygen states in the low valence nickelate $\text{La}_4\text{Ni}_3\text{O}_8$. *Physical Review X* **12**, 011055 (2022).
- [17] Schlappa, J. *et al.* Spin–orbital separation in the quasi-one-dimensional Mott insulator Sr_2CuO_3 . *Nature* **485**, 82–85 (2012).

- [18] Wohlfeld, K., Nishimoto, S., Haverkort, M. W. & van den Brink, J. Microscopic origin of spin-orbital separation in Sr_2CuO_3 . *Physical Review B* **88**, 195138 (2013).
- [19] Wohlfeld, K. Propagation of an orbitor in the antiferromagnets: theory and experimental verification. *arXiv preprint arXiv:1912.11363* (2019).
- [20] Kugel, K. I. & Khomskii, D. The Jahn-Teller effect and magnetism: transition metal compounds. *Soviet Physics Uspekhi* **25**, 231 (1982).
- [21] Martinelli, L. *et al.* Collective Nature of Orbital Excitations in Layered Cuprates in the Absence of Apical Oxygens. *Phys. Rev. Lett.* **132**, 066004 (2024).
- [22] Zhou, Z., Ye, W., Luo, H.-G., Zhao, J. & Chang, J. Robust superconducting correlation against inter-site interactions in the extended two-leg Hubbard ladder. *arXiv preprint arXiv:2303.14723* (2023).
- [23] Scheie, A. *et al.* Cooper-pair localization in the magnetic dynamics of a cuprate ladder. To be published. (2024).
- [24] Nocera, A. *et al.* Doping evolution of charge and spin excitations in two-leg Hubbard ladders: Comparing DMRG and FLEX results. *Physical Review B* **97**, 195156 (2018).